



Article

Highly Effective Electrochemical Water Splitting with Enhanced Electron Transfer between Ni₂Co Layered Double Hydroxide Nanosheets Dispersed on Carbon Substrate

Ziyi Wan ¹, Ping Tang ¹, Luwei Dai ¹, Yao Yang ¹, Lu Li ^{2,3} , Jun Liu ⁴, Min Yang ^{1,*} and Guowei Deng ^{1,*}

- ¹ Sichuan Provincial Key Laboratory for Structural Optimization and Application of Functional Molecules, College of Chemistry and Life Science, Chengdu Normal University, Chengdu 611130, China; m19950528261@163.com (L.D.)
- ² Key Laboratory of Auxiliary Chemistry and Technology for Chemical Industry, Ministry of Education, Shaanxi University of Science and Technology, Xi'an 710021, China
- ³ Shaanxi Collaborative Innovation Center of Industrial Auxiliary Chemistry and Technology, Shaanxi University of Science and Technology, Xi'an 710021, China
- ⁴ Medical Imaging Key Laboratory of Sichuan Province, North Sichuan Medical College, Nanchong 637000, China; ustbliujun@iccas.ac.cn
- * Correspondence: yangmin820525@126.com (M.Y.); guoweideng86@163.com (G.D.)

Abstract: A reasonable design of nickel-based catalysts is key to efficient and sustainable energy conversion. For electrocatalytic materials in alkaline electrolytes, however, atomic-level control of the active sites is essential. Moreover, the well-defined surface structure contributes to a deeper understanding of the catalytic mechanism. Here, we report the loading of defective nickel–cobalt layered double hydroxide nanosheets (Ni₂Co-LDH@C) after carbonization of silk. Under the precise regulation of the local coordination environment of the catalytic active site and the presence of defects, Ni₂Co-LDH@C can provide an ultra-low overpotential of 164.8 mV for hydrogen evolution reactions (HERs) at 10 mA cm⁻², exceeding that of commercial Pt/C catalysts. Density functional theory calculations show that Ni₂Co-LDH@C optimizes the adsorption energy of the intermediate and promotes the O–O coupling of the active site in the oxygen evolution reaction. When using Ni₂Co-LDH@Cs as cathodes and anodes to achieve overall water splitting, a low voltage of 1.63 V is required to achieve a current density of 10 mA cm⁻². As an ideal model, Ni₂Co-LDH@C has excellent water splitting properties and has the potential to develop water–alkali electrocatalysts.

Keywords: electrocatalyst; synergistic effect; carbonization of silk; overall water splitting



Citation: Wan, Z.; Tang, P.; Dai, L.; Yang, Y.; Li, L.; Liu, J.; Yang, M.; Deng, G. Highly Effective Electrochemical Water Splitting with Enhanced Electron Transfer between Ni₂Co Layered Double Hydroxide Nanosheets Dispersed on Carbon Substrate. *C* **2023**, *9*, 94. <https://doi.org/10.3390/c9040094>

Academic Editors: Claus Rebholz and Nikolaos Kostoglou

Received: 24 August 2023

Revised: 19 September 2023

Accepted: 28 September 2023

Published: 3 October 2023



Copyright: © 2023 by the authors. Licensee MDPI, Basel, Switzerland. This article is an open access article distributed under the terms and conditions of the Creative Commons Attribution (CC BY) license (<https://creativecommons.org/licenses/by/4.0/>).

1. Introduction

The development and search for modern, clean, economic, and sustainable energy technologies is an essential issue that needs to be addressed [1,2]. Hydrogen has a clear advantage as the most efficient and clean energy source of future concern [3–6]. Among the numerous hydrogen carriers and hydrogen production reactions, electrolytic water is considered to be a promising method for producing hydrogen with elevated purity due to its high efficiency and low cost [7–10]. Thus, HER catalysts with excellent performance and stability have been widely studied and developed. Precious metal catalysts such as Pt-based catalysts have shown excellent HER properties, but the rarity and high price of precious metals have limited their further development [11,12]. As a result, the search for inexpensive and efficient electrocatalysts that can replace precious metals has become a hot topic. The nanoflower-like N-dope carbon-encapsulated CoNiPt alloy structure with composition segregation exhibits excellent HER activity in alkaline media [13]. However, due to their conjugated electronic structure, graphene carbon atoms are not excellent electrocatalytic active sites and exhibit poor electrocatalytic activity in HER. Silk has a naturally occurring strong molecular fiber that contains C, N, O, H, and additional elements.

Compared to conventional substrate materials, elevated-temperature carbonized silk has better electrical conductivity, richer surface structure, higher stability and flexibility, and the self-supporting structural system gives a richer means of modification [14,15].

Carbon carriers are widely used in the field of electrocatalysis [16]. However, the inert surface of carbon materials usually causes the interaction force between the metal nanoparticles and the carbon surface to be too weak, which means that it is difficult to effectively regulate the electronic structure of metal nanoparticles and improve their catalytic activity, and it is difficult to effectively inhibit their agglomeration [17,18]. To solve the above key problems, a strategy of adjusting the π -conjugated structure of silk after carbonization to enhance the interaction between the carbon carrier and the loaded metal nanoparticles was proposed to achieve effective regulation of the electronic structure and catalytic activity of metal nanoparticles, and to improve their catalytic stability. [19] Composite nanoreactors with transition metal atoms and carbon substrates have been successfully constructed by doping carbonized silk with transition metal atoms such as Co and Ni [20]. The first-principle calculation shows that the modification of metal Co and Ni atoms can lead to the redistribution of the surface charge of carbon materials, and make carbon atoms around Co and Ni atoms appear to be electron-deficient, which significantly enhances the electron transfer from Co and Ni nanoparticles to carbon carriers [21]. The effect of interfacial charge rearrangement of C nanomaterials induced by metal Co and Ni atoms doping on HER catalytic performance was investigated. Overall, the adsorption of hydrogen by Co is quite strong, resulting in its low electrocatalytic decomposition activity for aquatic hydrogen. In contrast, the Ni site at the interface of the composite nanoreactor has a moderate hydrogen adsorption capacity and elevated hydrogen evolution activity. The Ni sites further away from the interface favor the splitting of water molecules and provide an efficient source of oxygen evolution reactions (OER) [22]. As a result, carbon materials were employed as a substrate for the synthesis of various Ni-Co electrocatalysts with different ratios. Among these catalysts, Ni₂Co-LDH@C exhibited exceptional HER performance in the alkaline. DFT calculations revealed that an increased amount of Ni facilitates the hydrolysis process during alkaline HER. It is noteworthy that the catalytic activity and surface oxygen content demonstrate a distribution pattern resembling a volcano shape, primarily attributed to Ni_{3d}-O_{2p} hybridization. The synergistic effect resulting from these factors enables the Ni₂Co-LDH@C catalyst to achieve an impressively low overpotential of 164.8/183.4 mV for HER/OER at a current density of 10 mA cm⁻², surpassing most previously reported catalysts in terms of performance advantages. In addition, when Ni₂Co-LDH@C is used as the cathode and anode for overall water splitting, it requires only a very low voltage of 1.82 V to for 50 mA cm⁻². Most importantly, its exceptional long-term stability in an alkaline environment gives it a possibility for actual use in overall water splitting.

2. Materials and Methods

2.1. Degumming of Silk Worm Cocoons

Due to the poor stability of sericin in the outer layer of the original silk, the silk needs to be degummed before use to obtain silk fibroin fiber. A certain amount of cocoons was weighed, they were split, the pupae was discard, and the cocoons were cut properly. The degummed silk was placed in 5 g/L Na₂CO₃ solution of 100:1, and the temperature of water bath was maintained at about 95 °C; after 30 min, the silk was removed. After repeated cleaning with distilled water, the silk was placed in an oven at 40 °C to dry for later use.

2.2. Synthesis of Ni_xCo_y-LDH@C

A certain quality of 17 mmol urea, 1 g PVP, Co(NO₃)₂·H₂O, and Ni(NO₃)₂·6H₂O were added into the beaker. Measures of 70 mL anhydrous ethanol and 10 mL deionized water were added to mix the raw materials well, then 0.5 g of degummed silk was added to the flask and refluxed in an oil bath at 90 °C for 10 h. After the solution was cooled to room temperature, the final products were collected by centrifugation, washed with deionized

water:ethanol = 1:1, and dried at 40 °C for 12 h. The dried products were annealed at 800 °C for 2 h at a heating rate of 2 °C min⁻¹. After calcination, 20 mg of the product was dispersed into 10 mL deionized water, and 10 mL 1.0 M HNO₃ solution was added drop by drop, then 10 mL 1.0 M NH₃·H₂O solution was added drop by drop. After ultrasonic treatment for 10 min, centrifuge washing was performed until the colution was neutral; then the samples were dried at 60 °C for 12 h to obtain the Ni_xCo_y LDH@C.

2.3. Structure Characterizations

A D/MAX2400 X-ray diffractometer produced by Company in Japan was adopted for X-ray diffraction (XRD) analysis; CuKα (X = 1.54 Å) was used as the radiation source. The operating voltage was 200 kV, current was 50 mA, 2θ was 10–80°, and the scanning rate was 10 min⁻¹. Raman spectroscopy analysis was used (Thermo Fisher Company, Waltham, MA, USA), in which the laser wavelength was 532 nm and the detection range was 0–2500 cm⁻¹. Morphology was analyzed by field emission scanning electron microscopy (FE-SEM, NOVA NanoSEM 450, American FEI Company, Hillsboro, OR, USA). Transmission electron microscopy (TEM) and high-resolution transmission electron microscopy (HRTEM) analysis were performed (Tecnai G2 F30S, American FEI Company). X-ray photoelectron spectroscopy (XPS) analysis was performed using ESCALAB 250 X-ray photoelectron spectroscopy (Thermo Fisher Company, Waltham, MA, USA) with Al Kα radiation.

2.4. Electrocatalytic Measurements

A three-electrode system was used for electrocatalytic test at room temperature (298.15 K). A Pt sheet was used as the counter electrode, the electrode Ag/AgCl was used as a counter reference. Ni_xCo_y-LDH@Cs were used as the working electrodes, relative to the standard hydrogen electrode (RHE). Voltage: $E_{\text{RHE}} = E_{\text{Ag/AgCl}} + 0.197 \text{ V} + 0.059 \times \text{pH}$. Linear sweep voltammetry (LSV) was used for the polarization curve of the electrochemical catalyst. The scanning rate was 2 mV/s. Stable tests were performed at the current density of 10 mA cm⁻². Electrochemical impedance spectroscopy (EIS) was used to measure the frequency range 0.1~100 kHz. Cyclic voltammetry (CV, scanning rate 50 mV/s) and the timing current method were used for the stability test. Electrochemical double-layer capacitance (C_{dl}) was measured by cyclic voltammetry curves at different scanning rates: CV test voltage range -0.05~0.45V (vs. RHE); scanning rate 5~100 mV/s. C_{dl} was calculated according to the following formula: $i_c = VC_{\text{dl}}$. Here, i_c is the exchange current (mA/cm²), V is the scanning rate (mV/s), and C_{dl} is the double layer capacitance (F/cm²). The turnover frequency range (TOF) was calculated at potentials of 1.0~1.5 V. The supporting information provides elaborate descriptions of the test methods employed for infrared spectroscopy, the techniques utilized for determining the total solution of water, and the calculation methods applied for density functional theory (DFT).

3. Results

3.1. Characterization of Electrocatalysts

Ni_xCo_y-LDH@C was prepared using the condensate reflux method. Then, NiCo-LDH@C was prepared by injecting nitrogen and calcining it at 800 °C. By adjusting the ratio of Ni/Co, catalysts with different Ni contents can be prepared (Figure 1a). They are labeled Ni₂Co-LDH@C, NiCo₂-LDH@C, and NiCo-LDH@C, according to the ratio of Ni/Co (Figure 1b). It can be seen that the main diffraction peaks of the sample before and after etching basically match the standard XRD cards (JCPDS:46-0943, 26-0408). The diffraction peaks of samples at 11.1°, 35.4°, and 48.9° are different from those of (003), (012), and (110), respectively. After loading with silk fibroin, diffraction peaks corresponding to the (003), (012), and (110) crystal planes of the sample still exist, and there are obvious diffraction peaks corresponding to silk fibroin at 31.2° and 52.5°, indicating that Ni₂Co-LDH was successfully loaded onto the silk and increased the layer spacing of LDH [23,24]. To understand the chemical valence states of each element in Ni₂Co-LDH@C, the XPS of Ni₂Co-LDH@C is given in Figure 2. The survey spectrums of Ni₂Co-LDH@C showed

that the sample material contains only Ni, Co, O, and C elements (Figure 1c). The XPS quantitative analysis results, as presented in Table S1, reveal Ni:Co ratios of 2.14:1.54 in NiCo-LDH@C, 5.43:2.45 in Ni₂Co-LDH@C, and 2.9:4.86 in NiCo₂-LDH@C, which impeccably align with the molar ratio indicated by the molecular formula. In the Ni_{2p} emission spectrum (Figure 1d), in addition to the two obvious satellite peaks, there are diffraction peaks with binding energies of 855.5 eV and 873.3 eV, corresponding to Ni_{2p3/2} and Ni_{2p1/2}, respectively, indicating the existence of only Ni²⁺. Gaussian fitting Co_{2p} high-resolution spectrum includes two satellite peaks and two spin orbit peaks (Figure 1e). In Co_{2p}, the peak values of binding energy at 780.5 eV and 796.2 eV correspond to Co³⁺, and the binding energies at 782.3 eV and 796.6 eV belong to Co²⁺. The appearance of Co³⁺ may be caused by the effect of oxygen in solution on the sample at high temperature [23–26]. The distribution of C in XPS data was roughly as follows: C-C 284.9 eV, C=O 288.3 eV, C-O 287.5 eV (as shown in Figure S1). IR spectra of Ni₂Co-LDH@C are shown in Figure 1f. The spectrum contained absorption vibration peaks of three types of functional groups. Two absorption peaks of 3426 and 1630 cm⁻¹ were caused by stretching vibration of hydroxyl O-H on the laminate and bending vibration of interlaminar water molecules. The strong absorption peak of 1404 cm⁻¹ can be attributed to the symmetric tensile vibration of Co-O, which indicates that the Co-O intercalation the low absorption peak is caused by lattice vibration of metal–oxygen bond (Ni-O or Co-O) [27–30]. Figure 1g shows the Raman spectra of Ni₂Co-LDH@C. The characteristic peaks of 1342, 1575, and 884 cm⁻¹ in the Raman spectrum correspond to D, G, and 2D peaks of the silk carbonized material, respectively. Among them, the D peak is the defect peak, which was caused by structural defects and disorder. In addition, the Raman spectra of the grown Ni₂Co-LDH@C materials demonstrate the vibration peaks of the Raman displacement at 459 and 517 cm⁻¹, which correspond to the tensile vibration of the Ni-OH bond and the symmetric stretching vibration mode of A_g in the Co-O bond, respectively [31,32]. In addition, by observing the Raman characteristic peak of the composite sample, the Ni₂Co-LDH@C composite structure was successfully synthesized.

In order to play a more efficient role, the conductivity of each carbonized silk fiber must be significantly enhanced. The current received by each component is required to efficiently conduct and bundle through the substrate material, thereby increasing its efficiency. Nickel and cobalt were loaded onto the silk by condensation reflux and then carbonized and modified with Ni₂Co-LDH. Efficient electrostatic materials were fabricated with better electrical conductivity, richer surface structure, and higher stability and flexibility than conventional substrate materials. Self-supporting structural systems give them richer means of modification [33,34]. Ni₂Co-LDH@C showed the SEM of two-dimensional rod-like morphology (Figure 2a,b), and aggregated Ni₂Co-LDH particles were observed on the surface of carbonized silk (Figure 2c). In addition, the atomic structure of Ni₂Co-LDH was revealed by HRTEM. The Ni and Co sites of the coordination were found to be uniformly anchored throughout the surface (Figure 2c). HRTEM was used to the study structural changes in the loaded carbonized silk. Figure 2e shows that the crystal spacing of Ni₂Co-LDH is 0.242 nm and 0.353 nm for the (111) and (002) crystal planes of Ni₂Co-LDH, respectively. Figure 2f shows that the two groups of nicely resolved lattice fringes at 0.353 nm and 0.261 nm belong to the (002) plane of NiCo-LDH, and 0.261 nm corresponds to the (012) crystal plane. The Ni₂Co-LDH@C with carbon atoms preserves the crystal structure of the NiCo-LDH, in agreement with the XRD results [35]. The EDS indicated a continuous decrease in the Ni content with the introduction of more Co atoms, indicating that some Ni atoms are replaced by Co atoms. The Wt% values of the Ni_xCo_y-LDH@C EDS analysis are presented in Table S2, showing the compositional ratios of NiCo-LDH@C (Ni/Co = 27.16:28.56), Ni₂Co-LDH@C (Ni/Co = 40.98:18.37), and NiCo₂-LDH@C (Ni:Co = 15.98:33.17). The Wt% analysis revealed that the molar ratios of Ni to Co are 1:1, 2:1, and 1:2, respectively, which closely align with the XPS result. In electrochemical performance tests, Ni₂Co-LDH@C was found to have the best catalytic performance (Figure 2g–i).

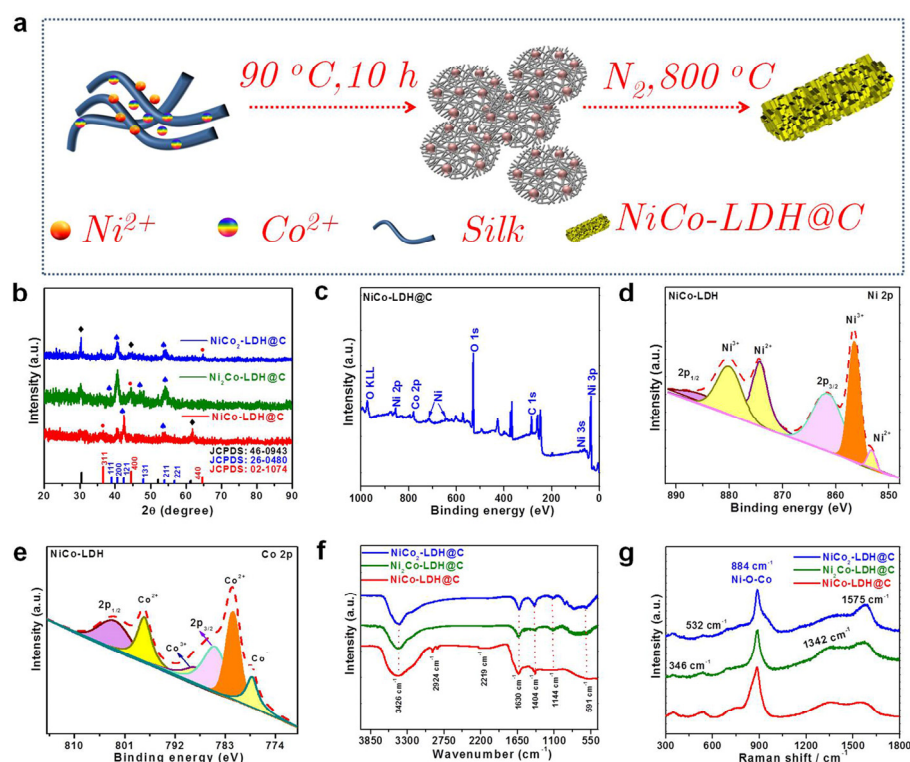


Figure 1. (a) Schematic diagram of the Ni₂Co-LDH@C preparation via a two-step method. (b) XRD pattern of the Ni_xCo_y-LDH@C; (c) XPS survey of the Ni₂Co-LDH@C catalysts; (d) the spectra of Ni_{2p}; (e) the spectra of Co_{2p}; (f) the FT-IR spectra of the Ni_xCo_y-LDH@C catalysts; (g) Raman spectra of the Ni_xCo_y-LDH@C catalysts.

3.2. Electrocatalytic Performance for the HER

The HER of the catalysts was studied in 1 mol/L KOH solution. Figure 3a showed NiCo-LDH@C, Ni₂Co-LDH@C, NiCo₂-LDH@C, and Pt/C. As expected, Ni₂Co-LDH@C showed the highest HER activity among the three synthesized catalysts, and the current density of 10 mA cm⁻² only needed 164.8 mV overpotential. However, NiCo₂-LDH@C and NiCo-LDH@C require 232 and 181.6 mV, respectively. Figure 3b shows the corresponding EIS for these catalysts. The R_{ct} of Ni₂Co-LDH@C was 3.32 Ω, indicating that the interface electron transfer rate of Ni₂Co-LDH@C was faster, and it could maintain a low overpotential even at a high current density. The Tafel of Ni₂Co-LDH@C was 113.9 mV dec⁻¹, which was lower than NiCo₂-LDH@C (242.8 mV dec⁻¹) and NiCo-LDH@C (230.49 mV dec⁻¹), 20 wt% Pt/C (38.7 mV dec⁻¹) (Figure 3c). Under the same current density of 10 mA cm⁻², the Ni₂Co-LDH@C catalyst exhibited significantly higher current density compared to catalysts with different molar ratios of components and outperformed commercial 20 wt% Pt/C catalysts. These results indicate that the prepared catalyst with a molar ratio of 2:1 demonstrates superior electrocatalytic activity for HER. The results showed that NiCo₂-LDH@C had the fastest reaction rate. In addition, Ni₂Co-LDH@C performance was better than many Ni-based catalysts (Table S3). These results indicated that the interfacial effect of Ni/Co heterostructure and the three-dimensional structure composed of carbon materials were conducive to enhancing the hydrogen evolution activity of the catalysts [36,37]. In order to compare the intrinsic activity of the catalysts, the electrochemical active surface area (ECSA) of catalytic activity was normalized. ECSA was proportional to the double layer capacitance (C_{dl}) of the catalyst (Figure S2), using CV curves at different scanning rates, the C_{dl} values of the NiCo-LDH@C, NiCo₂-LDH@C, and Ni₂Co-LDH@C can be calculated as 4.65 mF cm⁻², 3.80 mF cm⁻², and 26.10 mF cm⁻², respectively. Ni₂Co-LDH@C had a lower activation energy of only 6.6 kJ/mol compared to the remaining two catalysts. It was considerably smaller than NiCo₂-LDH@C (11 kJ/mol), NiCo-LDH@C (7.2 kJ/mol),

and Ni₂Co-LDH (12.8 kJ/mol), and the adsorption of hydrogen by Co is overly strong, resulting the low activity of electrocatalytic decomposition of aquatic hydrogen. Comparing the electrocatalytic activities of several catalysts with current densities of 10 mA·cm⁻², 50 mA/cm⁻², and 100 mA·cm⁻², Ni₂Co-LDH@C had the lowest overpotential (Figure 3f). The Ni₂Co-LDH@C catalyst had the lowest hydrogen evolutionary excess potential compared to similar published catalysts. To verify the stability of the sample, after circulating the catalyst for 1000 cycles, the coincidence degree of the curve elevated and practically no shift is present, indicating perfect stability. As shown in Figure 3i, at the initial current density of 10 mA·cm⁻², the sample showed no obvious attenuation after 12 h.

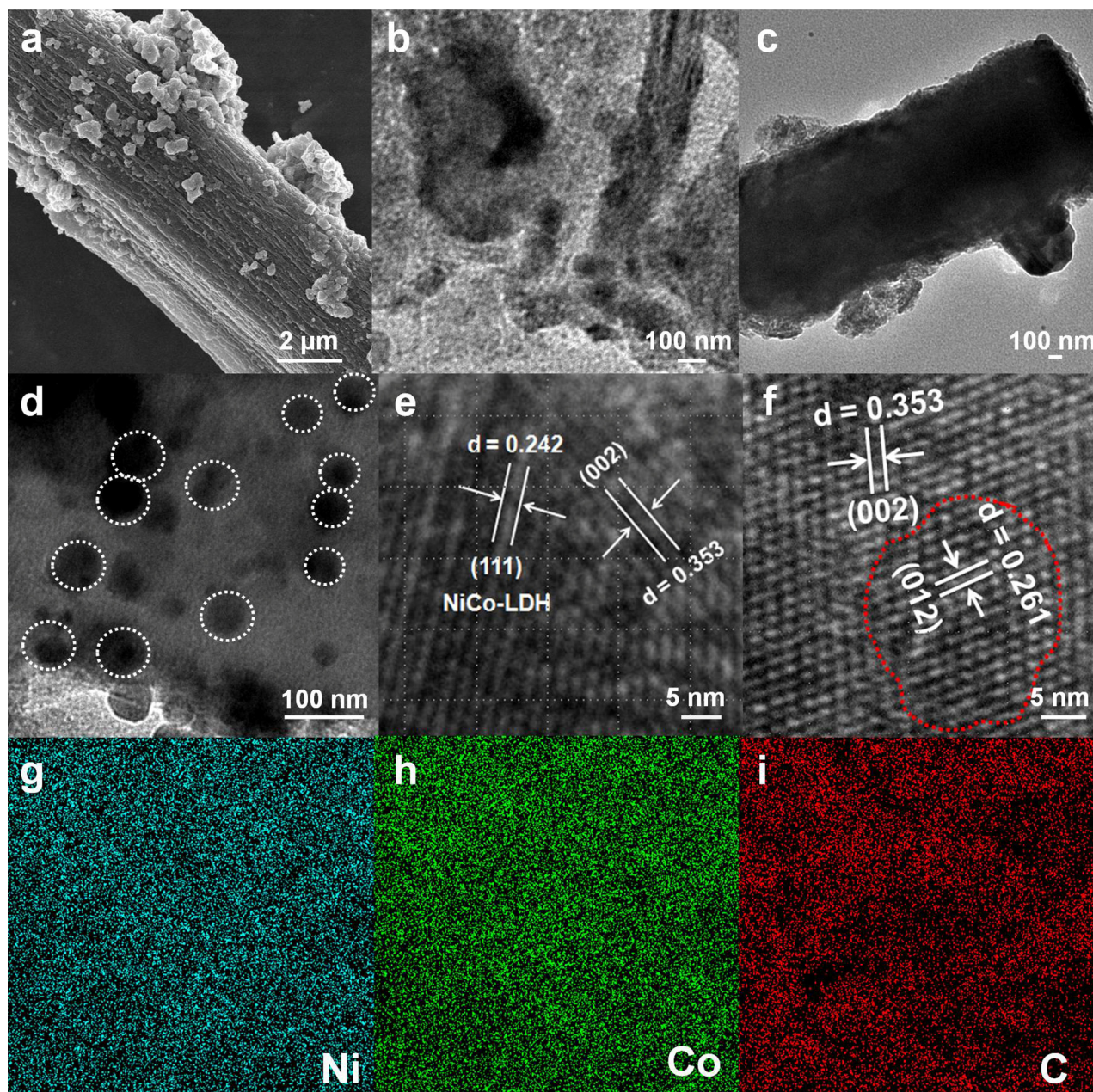


Figure 2. (a) SEM of the Ni₂Co-LDH@C catalysts. Scale bar: 2 μ m. (b) TEM of the carbonization of silk. (c,d) TEM of the Ni₂Co-LDH@C catalysts. Scale bar: 100 nm. (e) HRTEM of the Ni₂Co-LDH catalysts. (f) HRTEM of the Ni₂Co-LDH@C catalysts. Scale bar: 5 nm. (g–i) Mapping of Ni, Co, and C elements.

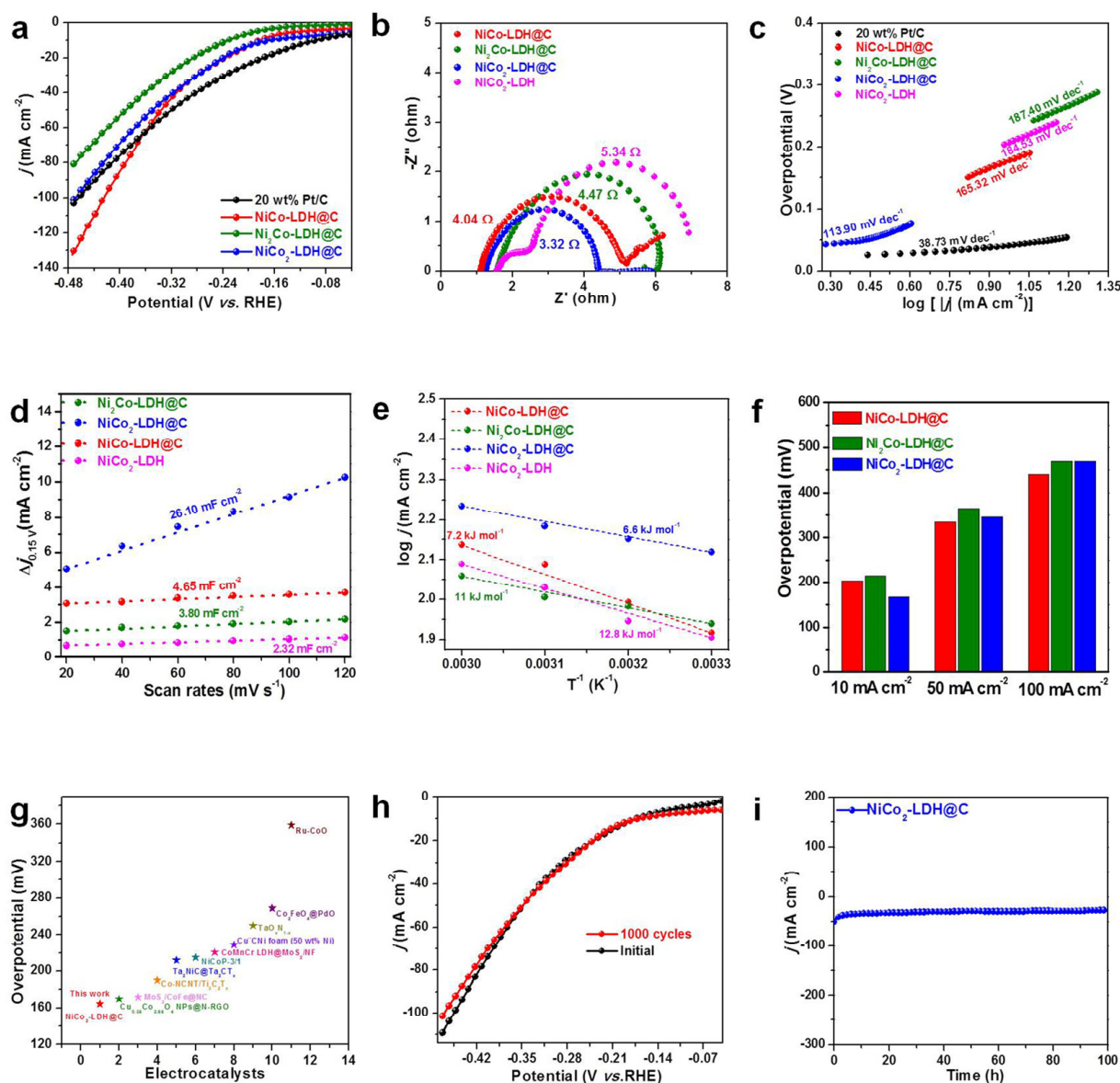


Figure 3. (a) HER LSV curves of NiCo-LDH@C, Ni₂Co-LDH@C, and NiCo₂-LDH@C at 20 wt% Pt/C/NF. (b) EIS tests of NiCo-LDH@C, Ni₂Co-LDH@C, and NiCo₂-LDH@C. (c) Tafel plots of NiCo-LDH@C, Ni₂Co-LDH@C, and NiCo₂-LDH@C. (d) ECSA of NiCo-LDH@C, Ni₂Co-LDH@C, and NiCo₂-LDH@C. (e) E_a of NiCo-LDH@C, Ni₂Co-LDH@C, and NiCo₂-LDH@C. (f) The comparisons of overpotential at 10 mA cm⁻² (η_{10}) and 50 mA cm⁻² of NiCo-LDH@C, Ni₂Co-LDH@C, and NiCo₂-LDH@C. (g) HER performance comparison. (h) Polarization curves for the Ni₂Co-LDH@C before and after 1000 cycles. (i) The chronoamperometric curves of Ni₂Co-LDH@C for 100 h.

3.3. Electrocatalytic Performance for the OER

The OER catalytic activity of the samples was evaluated in the 1.0 mol/L KOH electrolyte. Figure 4a shows the polarization curves of samples obtained by linear sweep voltammetry (LSV). As can be seen from the polarization curves, the OER catalytic performance of the samples obtained is gradually enhanced with the difference of Ni/Co ratio. When Ni:Co = 2:1, it shows the optimal catalytic activity. When the current density is 10 mA·cm⁻², the overcurrent potential is only 183.4 mV. Ni₂Co-LDH@C performance was better than many Ni-based catalysts (Table S4). However, when Ni:Co = 1:1, the catalytic activity of the obtained sample suddenly decreased, which may be due to the collapse of the NiCo-LDH structure, resulting in a sharp reduction in the specific surface area. The interfacial charge transfer resistance (R_{ct}) controls the charge transfer efficiency of interfacial

reaction. As shown in Figure 4b, the R_{ct} of Ni₂Co-LDH@C was 2.95 Ω , indicating that the interface electron transfer rate of Ni₂Co-LDH@C was faster in the OER reaction. The Tafel slope reflected the kinetic performance of OER. In general, the smaller the Tafel slope is, the better the kinetic performance of the catalyst. As can be seen from Figure 4c, the slope of Tafel decreased from 169 mV dec⁻¹ to 108.27 mV dec⁻¹ with a different Ni:Co ratio, indicating that the introduction of Ni ions can improve the dynamic performance of Ni₂Co-LDH@C. In order to compare the intrinsic activity of the catalysts, the E_a of catalytic activity was normalized, as shown in Figure 4d. The defect-rich structure and metal/oxide interface substantially improved the intrinsic activity of the catalyst: its E_a was Ni₂Co-LDH@C < NiCo₂-LDH@C < NiCo-LDH@C < Ni₂Co-LDH. Compared with similar published catalysts, the Ni₂Co-LDH@C catalyst had the lowest oxygen evolution overpotential (Figure 4e). The OER overpotential was compared at different current densities (10, 50, 100 mA·cm⁻²). The results showed that the Ni₂Co-LDH@C catalyst had the lowest excess potential at different current densities, suggesting that Ni₂Co-LDH@C had better catalytic activity for oxygen evolution (Figure 4f). Figure 4g shows the multistep timing voltage analysis curves; similarly to the results of OER, its voltage does not change significantly as the current density increases sequentially from -30 to -300 mA·cm⁻², and each time it increases by -30 mA cm⁻² and stays for 500 s. By coupling Ni₂Co-LDH@C, NiCo₂-LDH@C, and NiCo-LDH@C for the heterogeneous structure, Ni:Co not only makes use of the bifunctional properties, but also improves the intrinsic activity of the catalyst through the interface effect [38,39]. In addition to catalytic activity and kinetic properties, stability is also an important factor in evaluating the performance of catalysts. The stability of Ni₂Co-LDH@C characterized by loop test, after 1000 cycles, the curves basically coincide (Figure 4h). At the initial current density of 10 mA·cm⁻², the current density of Ni₂Co-LDH@C can remain after 12 h (Figure 4i), indicating that it has excellent long-term stability in OER catalytic reaction.

3.4. Overall Water Splitting Performance

Ni₂Co-LDH@C||Ni₂Co-LDH@C were used as both cathode and anode catalysts for the water splitting reaction. Figure 5a showed the polarization curves of its catalyst reaction. Ni₂Co-LDH@C||Ni₂Co-LDH@C required only 1.63, 1.82, and 1.94 V to obtain current densities of 10, 50, and 100 mA cm⁻², respectively (Figure 5b). In addition, the performance of the Ni₂Co-LDH@C||Ni₂Co-LDH@C catalyst was better than others reported (Figure 5c). The above results indicate that Ni₂Co-LDH@C||Ni₂Co-LDH@C had excellent HER and OER stability. The intrinsic catalytic performance of Ni₂Co-LDH@C||Ni₂Co-LDH@C electrode was evaluated by oxygen turnover frequency. The cyclic voltammetry diagram showed the linear relationship with the scanning rate. The cyclic voltammetry (Figures S3–S5) showed that the oxidation peak of the sample had a linear relationship with the scanning rate, after fitting with LSV (Figure 5d). Table S5 shows that the oxygen turnover frequency of NiCo-LDH@C was 0.0103 s⁻¹ and that of NiCo₂-LDH@C was 0.0216 s⁻¹. Ni₂Co-LDH@C reached 0.0597 mol O₂ s⁻¹ under the overpotential of 190.6 mV. Table S6 shows the oxygen turnover frequency of NiCo₂-LDH@C||NiCo₂-LDH@C, which reached 0.0615 mol O₂ s⁻¹ under the overpotential of 181.6 mV (Figure 5e). The catalysts with a three-dimensional array structure supported on the loose and porous surface of the carbon materials facilitated the exposure of the active site and the escape of bubbles as well as contact with the electrolyte. Under the same conditions, the performance of nickel-based transition metal electrocatalysts is better than most of the previously reported nickel-based transition metal electrocatalysts (Table S7). The voltage test experiment (Figure 5h) shows that the Ni₂Co-LDH@C||Ni₂Co-LDH@C electrodes had good stability of total solution water at 1.66 V, and the potential change can be ignored. Figure 5f shows the overall water splitting performance of the device over 100 h (producing O₂) and the cathode (producing H₂); the two-electrode catalyst showed good stability.

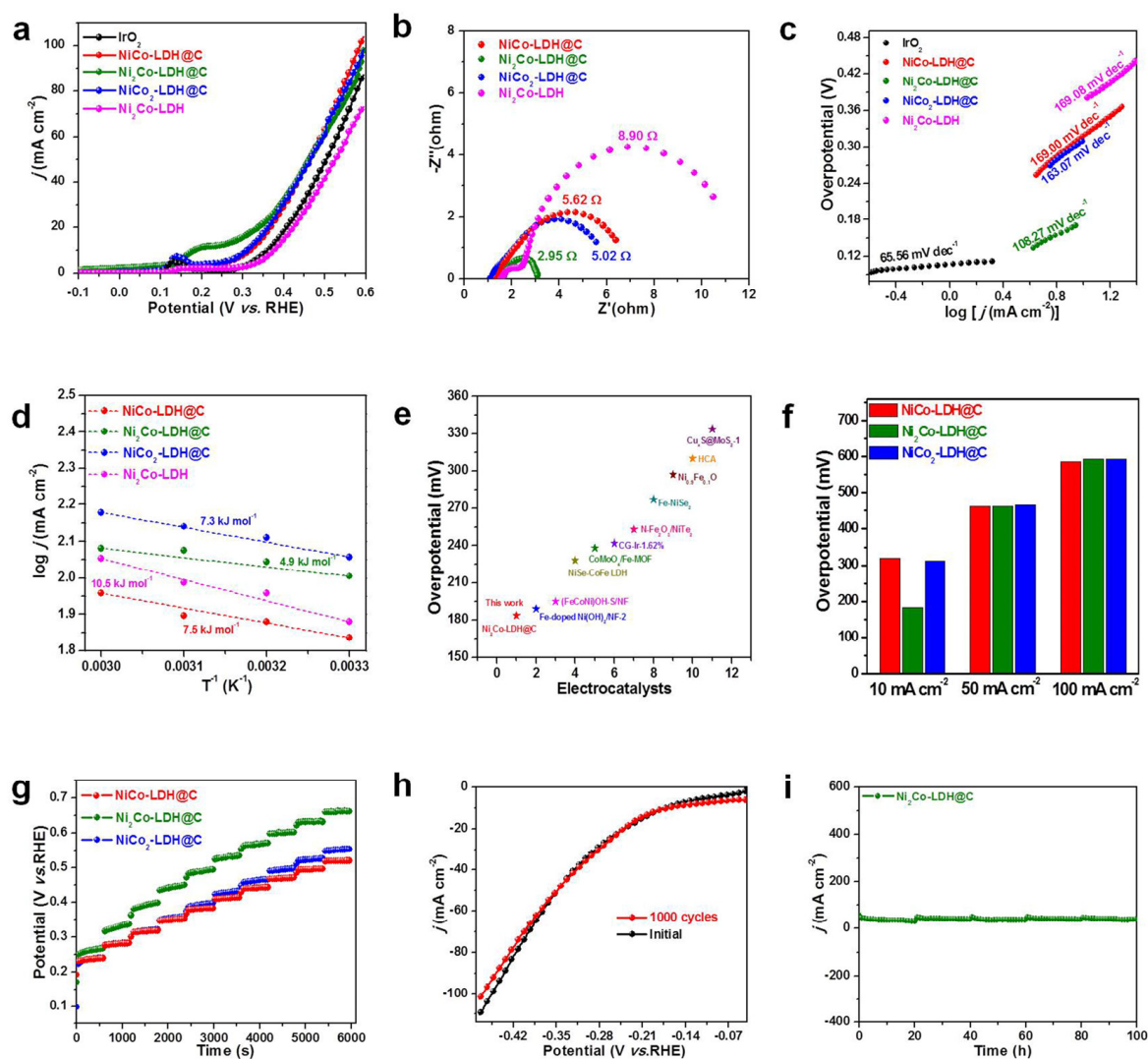


Figure 4. (a) OER LSV curves of NiCo-LDH@C, Ni₂Co-LDH@C, NiCo₂-LDH@C, and IrO₂. (b) EIS curves of NiCo-LDH@C, Ni₂Co-LDH@C, NiCo₂-LDH@C, and IrO₂. (c) Tafel plots of NiCo-LDH@C, Ni₂Co-LDH@C, and NiCo₂-LDH@C. (d) Ea of NiCo-LDH@C, Ni₂Co-LDH@C, and NiCo₂-LDH@C. (e) OER performance comparison. (f) The comparisons of overpotential at 10 mA cm⁻² (η_{10}) and 50 mA cm⁻² of NiCo-LDH@C, Ni₂Co-LDH@C, and NiCo₂-LDH@C. (g) CP plots on the catalyst. (h) Polarization curves for the Ni₂Co-LDH@C before and after 1000 cycles. (i) The chronoamperometric curves of Ni₂Co-LDH@C for 100 h.

3.5. Theoretical Calculation Analysis

Ni₂Co-LDH@C had a higher electron density than Ni₂Co-LDH in the Fermi level, indicating that Ni₂Co-LDH@C had faster electron transfer, thereby improving its electrical conductivity and showing enhanced catalytic activity, which was consistent with experimental tests (Figure 6a). The C is introduced into Ni₂Co-LDH in alkaline media to improve HER performance. This was investigated using DFT models. The adsorption of H₂O on catalyst surface and the cleavage of H-OH bond with OH* and H* were the key steps of the HER reaction under alkaline conditions. The mechanism of the excellent HER properties was investigated by using the Gibbs free energies of H₂O (ΔG_{H_2O}) and H* (ΔG_{H^*}). The ΔG_{H^*} value of Ni₂Co-LDH@C was tiny, indicating that the supporting carbon materials were conducive to improving HER performance (Figure 6b). The responsible for the excellent HER performance was explained in Figure 6c. Since the weak adsorption of HER to intermediates is the key factor for its elevated activity, the physical mechanism of hydrogen evolution discussed by studying the electronic structure of Ni₂Co-LDH@C (Figure 6c). In general, the

OER pathway is a four-electron transfer step, including: $\text{H}_2\text{O} \rightarrow * \text{OH} + (\text{H}^+ + \text{e}^-)$, $* \text{OH} \rightarrow * \text{O} + (\text{H}^+ + \text{e}^-)$, $* \text{O} + \text{H}_2\text{O} \rightarrow * \text{OOH} + (\text{H}^+ + \text{e}^-)$ and $* \text{OOH} \rightarrow \text{O}_2 + (\text{H}^+ + \text{e}^-)$ (Figure 6d) [40].

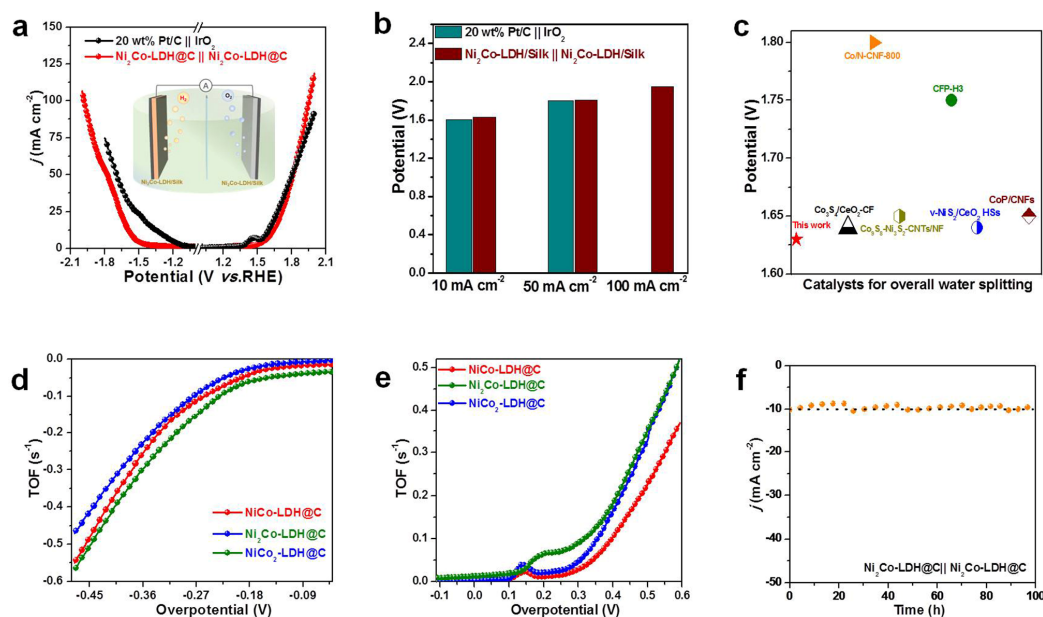


Figure 5. (a) LSV curves of 20 wt% Pt/C || IrO₂ and Ni₂Co-LDH@C || Ni₂Co-LDH@C in a two-electrode configuration in 1 M KOH. (b) The comparisons of potential at 10 mA cm⁻², 50 mA cm⁻² and 100 mA cm⁻² of Ni₂Co-LDH@C || Ni₂Co-LDH@C. (c) Comparison performance of overall water splitting. (d) The calculated TOF values of the NiCo-LDH@C, Ni₂Co-LDH@C, and NiCo₂-LDH@C varied with the HER potentials. (e) The calculated TOF values of the NiCo-LDH@C, Ni₂Co-LDH@C, and NiCo₂-LDH@C varied with the OER potentials. (f) The stability measurements of Ni₂Co-LDH@C || Ni₂Co-LDH@C in 1 M KOH.

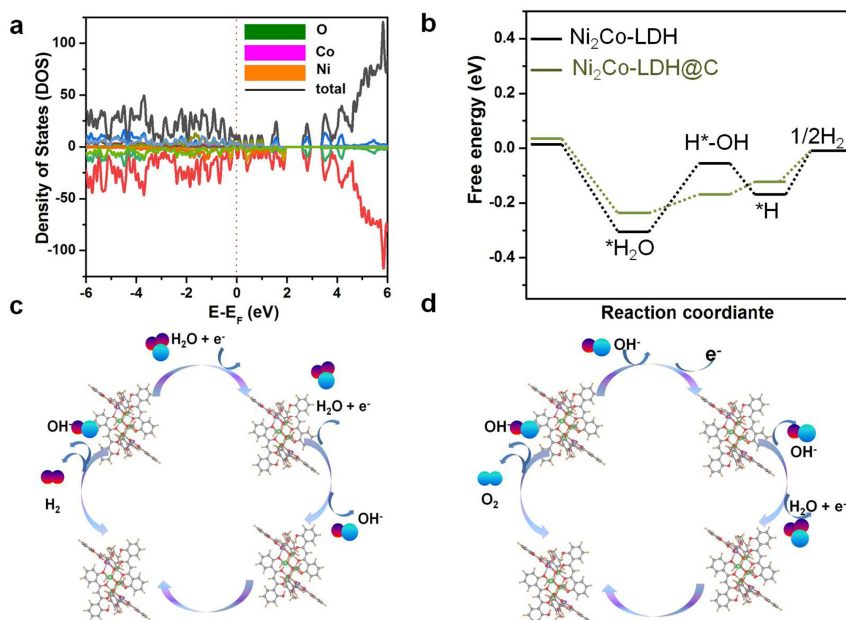


Figure 6. (a) DOS of Ni₂Co-LDH@C; (b) Gibbs free-energy diagrams of HER intermediates for Ni₂Co-LDH@C; (c) Schematic diagram of HER mechanism; (d) Schematic diagram of OER mechanism.

4. Conclusions

In summary, a novel electrocatalytic synthesis strategy has been described for the self-sustained stabilization of defective NiCo-LDH-active sites in carbon materials. Based

on the precise tuning of the active site Ni:Co, Ni₂Co-LDH@C offers superior HER and OER properties with low excess potential, elevated current density, and long-term persistence in alkaline media. The well-defined structure of the catalyst also allows for a fundamental study of the reaction steps and dynamics of the HER and OER reactions. For example, DFT calculations show that Ni₂Co-LDH@C promotes favorable regulation of the H₂ adsorption energy by HER and O-O coupling to the OER. This work not only develops a simple and practical strategy for the synthesis of Ni₂Co-LDH@C, but also theoretically/experimentally confirms the key role of carbon materials as self-supporting catalysts in the unexpected optimization of electrocatalytic activity, opening up new opportunities for the development of efficient and stable electrocatalysts, and potentially for the development of improved commercial water splitting processes.

Supplementary Materials: The following supporting information can be downloaded at: <https://www.mdpi.com/article/10.3390/c9040094/s1>, Figure S1: XPS spectra of C_{1s} XPS spectra; Figure S2: Cyclic voltammograms of Ni_xCo_y-LDH@C; Figures S3–S5: Cyclic voltammograms of Ni_xCo_y-LDH@C; Table S1: Comparison of HER performance; Table S2: Comparison of OER performance; Table S3: OER-TOF of the catalyst at the specific overpotential; Table S4: OER-TOF of the catalyst at the specific overpotential; Table S5: Comparison of overall splitting water performance. Table S6: HER-TOF determined at 167.6 mV (vs. RHE). Table S7: The overall performances of the as-prepared electrode and other electrodes with electrocatalysts in 1.0 M KOH.

Author Contributions: Conceptualization, Z.W. also processed the experimental data, performed the analysis. P.T. partially contributed to the collection of data. L.D. processed the experimental data. Y.Y. processed the experimental data. L.L. and J.L. funding acquisition. M.Y. was involved in the planning, formulation, design, and implementation of the research. G.D. formulation, design, and implementation of the research. All authors have read and agreed to the published version of the manuscript.

Funding: This research received the Open Foundation of Key Laboratory of Auxiliary Chemistry and Technology for Chemical Industry, Ministry of Education, Shaanxi University of Science and Technology (KFKT2021-06), National Undergraduate Training Program for Innovation and Entrepreneurship (S202314389160). Supported by the Opening Project of Structural Optimization and Application of Functional Molecules Key Laboratory of Sichuan Province (2023GNFZ-02). Medical Imaging Key Laboratory of Sichuan Province, North Sichuan Medical College, Nanchong, Sichuan, China, 637000 (MIKL202204).

Data Availability Statement: Data are contained within the article.

Acknowledgments: D/MAX2400 X-ray diffractometer produced by Company in Japan was adopted for X-ray diffraction (XRD) analysis, with CuK α ($\lambda = 1.54 \text{ \AA}$) is the radiation source; operating voltage was 200 kV, current was 50 mA, 2θ is $10\text{--}80^\circ$, and the scanning rate was 10 min^{-1} . Raman spectroscopy (Thermo Fisher Company in the United States); laser wavelength was 532 nm and the detection range was $0\text{--}2500 \text{ cm}^{-1}$. Morphology was analyzed by field emission scanning electron microscopy (FE-SEM, NOVA NanoSEM 450, American FEI Company). Transmission electron microscope (TEM) and high-resolution transmission electron microscope (HRTEM) analysis used by Tecnai G2 F30S (American FEI company). X-ray photoelectron spectroscopy (XPS) analysis was performed using ESCALAB 250 X-ray photoelectron spectroscopy (Thermo Fisher Company) with Al K α radiation.

Conflicts of Interest: The authors declare no conflict of interest.

References

1. Sun, T.; Tang, Z.Y.; Zang, W.J.; Li, Z.J.; Li, J.; Li, Z.H.; Cao, L.; Rodriguez, J.S.D.; Mariano, C.O.M.; Xu, H.; et al. Ferromagnetic single-atom spin catalyst for boosting water splitting. *Nat. Nanotechnol.* **2023**, *18*, 763–771. [[CrossRef](#)] [[PubMed](#)]
2. Zang, Y.; Lu, D.Q.; Wang, K.; Li, B.; Peng, P.; Lan, Y.Q.; Zang, S.Q. A pyrolysis-free Ni/Fe bimetallic electrocatalyst for overall water splitting. *Nat. Commun.* **2023**, *14*, 1792. [[CrossRef](#)] [[PubMed](#)]
3. Zhu, J.; Du, Q.X.; Khan, M.A.; Zhao, H.B.; Fang, J.H.; Ye, D.X.; Zhang, J.J. 2D porous Co-Mo nitride heterostructures nanosheets for highly effective electrochemical water splitting. *Appl. Surf. Sci.* **2023**, *623*, 156989. [[CrossRef](#)]
4. Kharabe, G.P.; Illathvalappil, R.; Barik, S.; Kanheerampockil, F.; Walko, P.S.; Bhat, S.K.; Devi, R.N.; Kurungot, S. A cobalt-manganese modified theophrastite phase of nickel hydroxide nanoflower arrays on nickel foam as a self-standing bifunctional electrode for overall water electrolysis. *Sustain. Energy Fuels* **2023**, *7*, 2428–2440. [[CrossRef](#)]

5. Liu, Z.Y.; Li, Y.; Peng, S.S.; Huang, J.; Su, B.L.; Gao, K.; Zhou, S.; Gao, Z.J.; Chen, T. A comprehensive melamine sponge decorated with 3D flowerlike Ag/NiCo-layered double hydroxide for wastewater remediation. *J. Environ. Chem. Eng.* **2022**, *10*, 108447. [[CrossRef](#)]
6. Wijaya, R.A.; Suseno, A.; Lusiana, R.A.; Septina, W.; Harada, T. Synthesis of CuInS₂ thin film photocathode with variation of sulfurization sources and Pt-In₂S₃ modification for photoelectrochemical water splitting. *J. Electroanal. Chem.* **2023**, *945*, 117683.
7. Hu, Y.H.; Shen, T.Y.; Song, Z.H.; Wu, Z.H.; Bai, S.; Liu, G.H.; Sun, X.L.; Wang, Y.Y.; Hu, S.Y.; Zheng, L.R.; et al. Atomic Modulation of Single Dispersed Ir Species on Self-Supported NiFe Layered Double Hydroxides for Efficient Electrocatalytic Overall Water Splitting. *ACS Catal.* **2023**, *13*, 11195–11203. [[CrossRef](#)]
8. Lee, D.E.; Moru, S.; Reddy, K.P.; Jo, W.K.; Tonda, S. Bimetallic Cu–Ni core–shell nanoparticles anchored N-doped reduced graphene oxide as a high-performance bifunctional electrocatalyst for alkaline water splitting. *Appl. Surf. Sci.* **2023**, *622*, 156928. [[CrossRef](#)]
9. Liu, Z.; Liu, Y.X.; He, H.W.; Shao, H.B.; Zhang, Y.; Li, J.; Cai, W.W. Valence regulation of Ru/Mo₂C heterojunction for efficient acidic overall water splitting. *Electrochim. Acta* **2023**, *443*, 141920. [[CrossRef](#)]
10. Nguyen, T.H.T.; Zarkua, Z.; Chinnappa, C.V.; Hu, W.J.; Sree, S.P.; Grandjean, D.; Pant, D.; Janssens, E. Co_{3–x}Fe_xO₄ inverse opals with tunable catalytic activity for high-performance overall water splitting. *Nanoscale* **2023**, *15*, 10306–10318. [[CrossRef](#)]
11. Luo, J.B.; Zhou, Y.; Wang, X.Z.; Gu, Y.F.; Liu, W.L.; Wang, S.T.; Zhang, J. CoMoO₄-CoP/NC heterostructure anchored on hollow polyhedral N-doped carbon skeleton for efficient water splitting. *J. Colloid Interface Sci.* **2023**, *648*, 90–101. [[CrossRef](#)]
12. Pan, Y.D.; Gao, J.K.; Lv, E.J.; Li, T.T.; Xu, H.; Sun, L.; Nairan, A.; Zhang, Q.C. Integration of Alloy Segregation and Surface Co–O Hybridization in Carbon-Encapsulated CoNiPt Alloy Catalyst for Superior Alkaline Hydrogen Evolution. *Adv. Funct. Mater.* **2023**, *33*, 2303833. [[CrossRef](#)]
13. Jing, F.L.; Pi, Y.Y.; Zhao, C.X.; Zhou, H.; Luo, S.Z.; Fang, W.H. Constructing highly stable dendritic silica-wrapped NiCo/carbon nanotubes architecture for hydrogen production. *Mater. Today Sustain.* **2022**, *19*, 100183. [[CrossRef](#)]
14. Liu, B.H.; Li, S.Y.; Wang, T.Q.; Yang, Y.; Wang, L.X.; Zhang, X.; Liu, Z.C.; Niu, L.W. Construction of CoFe bimetallic phosphide microflowers electrocatalyst for highly efficient overall water splitting. *Catal. Commun.* **2023**, *175*, 106607. [[CrossRef](#)]
15. Li, N.; Qu, S.J.; Qin, F.F.; Li, H.Y.; Shen, W.Z. Construction of P,N-codoped carbon shell coated CoP nanoneedle array with enhanced OER performance for overall water splitting. *Int. J. Hydrogen Energy* **2023**, *48*, 27215–27230. [[CrossRef](#)]
16. Li, N.; Qu, S.J.; Ma, J.J.; Shen, W.Z. Core-shell-structured CoS₂@N-doped carbon nanoneedle array as an efficient bifunctional electrocatalyst for overall water splitting. *Int. J. Hydrogen Energy* **2023**, *48*, 180–195. [[CrossRef](#)]
17. Yang, M.; Cui, Z.; Wang, Q.H.; Yin, J.F.; Yang, L.; Wang, O.; Deng, G.W. Improvement of specific capacitance and rate performance of NiWO₄ synthesized through modified chemical precipitation. *J. Mater. Sci. Mater. Electron.* **2021**, *32*, 12232–12240. [[CrossRef](#)]
18. He, X.D.; Han, X.; Zhou, X.Y.; Chen, J.D.; Wang, J.; Chen, Y.; Yu, L.H.; Zhang, N.; Li, J.; Wang, S.; et al. Electronic modulation with Pt-incorporated NiFe layered double hydroxide for ultrastable overall water splitting at 1000 mA cm⁻². *Appl. Catal. B Environ.* **2023**, *331*, 122683. [[CrossRef](#)]
19. Chen, K.; Cao, Y.H.; Yadav, S.; Kim, G.C.; Han, Z.; Wang, W.M.; Zhang, W.J.; Dao, V.; Lee, I. Electronic structure reconfiguration of nickel–cobalt layered double hydroxide nanoflakes via engineered heteroatom and oxygen-vacancies defect for efficient electrochemical water splitting. *Chem. Eng. J.* **2023**, *463*, 142396. [[CrossRef](#)]
20. Peng, M.W.; Zhao, B.; Shi, D.L.; Wang, Y.W.; Li, D.; Liang, W.K.; Yang, H.; Liang, Z.Q.; Sun, Y.H.; Jiang, L. Enabling high loading of well-dispersed Ni₂CoP₂ catalysts on a 3D-printed electrode for efficient electrocatalysis. *J. Mater. Chem. A* **2023**, *11*, 15394. [[CrossRef](#)]
21. Li, G.L.; Miao, Y.Y.; Qiao, X.Y.; Wang, T.Y.; Deng, F. Engineering edge sites based on NiS₂/MoS₂/CNTs heterojunction catalyst for overall water splitting. *Appl. Surf. Sci.* **2023**, *615*, 156309. [[CrossRef](#)]
22. Fei, L.S.; Sun, H.N.; Xu, X.M.; Li, Y.; Ran, R.; Zhou, W.; Shao, Z.P. Understanding the bifunctional catalytic ability of electrocatalysts for oxygen evolution reaction and urea oxidation Reaction: Recent advances and perspectives. *Chem. Eng. J.* **2023**, *471*, 144660. [[CrossRef](#)]
23. Yang, H.S.; Fu, Q.; Hou, Y.; Yu, J.X.; Tong, Y.J.; Li, N.; Zhong, H.J.; Zhu, F.; Wang, J.H.; Hao, Z.P.; et al. Ultrahigh surface area of single-atom iron nanosheets assists in the efficient utilization of reactive oxygen species in the peroxydisulfate activation process for pollutant removal. *Environ. Sci. Nano* **2023**, *10*, 1152. [[CrossRef](#)]
24. Huang, Q.P.; Jiang, M.J.; Li, Y.Y.; Liang, C.; Tang, Y.M.; Xie, F.Y.; Yang, M.; Deng, G.W. Construction of Mn_xCo_yO₄/Ti electrocatalysts for efficient bifunctional water splitting. *Dalton Trans.* **2022**, *51*, 9085. [[CrossRef](#)]
25. Sun, A.; Qiu, Y.L.; Wang, Z.X.; Cui, L.; Xu, H.Z.; Zheng, X.Z.; Xu, J.T.; Liu, J.Q. Interface engineering on super-hydrophilic amorphous/crystalline NiFe-based hydroxide/selenide heterostructure nanoflowers for accelerated industrial overall water splitting at high current density. *J. Colloid Interface Sci.* **2023**, *650*, 573–581. [[CrossRef](#)]
26. Qiu, S.P.; Zhang, B.J.; Wang, X.; Huang, J.Z.; Zhao, G.; Ding, M.; Xu, X.J. Interface strong-coupled 3D Mo–NiS@Ni–Fe LDH flower-cluster as exceptionally efficient electrocatalyst for water splitting in wide pH range. *J. Colloid Interface Sci.* **2023**, *641*, 277–288. [[CrossRef](#)]
27. Nayem, S.M.A.; Islam, S.; Aziz, M.A.; Ahammad, A.J.S. Mechanistic insight into hydrothermally prepared molybdenum-based electrocatalyst for overall water splitting. *Electrochim. Acta* **2023**, *445*, 142050. [[CrossRef](#)]

28. Ma, G.Y.; Ye, J.T.; Qin, M.Y.; Sun, T.Y.; Tan, W.X.; Fan, Z.H.; Huang, L.F.; Xin, X. Mn-doped NiCoP nanopin arrays as high-performance bifunctional electrocatalysts for sustainable hydrogen production via overall water splitting. *Nano Energy* **2023**, *115*, 108679. [[CrossRef](#)]
29. Gu, R.Z.; Zhou, T.; Wang, Z.H.; Chen, Z.; Tao, J.W.; Fan, Z.W.; Guo, L.Y.; Liu, Y.S. Mo/P doped NiFeSe as bifunctional electrocatalysts for overall water splitting. *Int. J. Hydrogen Energy* **2023**, *48*, 27642–27651. [[CrossRef](#)]
30. Gao, Y.H.; He, W.J.; Cao, D.; Wang, F.Q.; Li, Y.; Hao, Q.Y.; Liu, C.C.; Liu, H. Mo-Doped Ni₃S₂ Nanosheet Arrays for Overall Water Splitting. *ACS Appl. Nano Mater.* **2023**, *6*, 6066–6075. [[CrossRef](#)]
31. You, T.; Deng, K.; Liu, P.; Lv, X.B.; Tian, W.; Li, H.J.; Ji, J.Y. Synergism of NiFe layered double hydroxides/phosphides and Co-NC nanorods array for efficient electrocatalytic water splitting. *Chem. Eng. J.* **2023**, *470*, 144348. [[CrossRef](#)]
32. Ning, S.L.; Wu, Q.K.; Zhu, Y.G.; Liu, S.L.; Zhou, W.; Mi, L.; Zhou, K.; Zhao, D.K.; Zhang, X.Y.; Wang, N. N-doped carbon nanowire array confined cobalt phosphides as efficient bifunctional electrocatalysts for water splitting. *Inorg. Chem. Front.* **2023**, *10*, 2145–2153. [[CrossRef](#)]
33. Xie, Y.H.; Feng, Y.M.; Jin, S.Y.; Li, C.; Li, C.S.; Sun, Y.; Luo, F.; Yang, Z.H. Nickel-doped iridium echinus-like nanosheets for stable acidic water splitting. *Chem. Commun.* **2023**, *59*, 8404–8407. [[CrossRef](#)] [[PubMed](#)]
34. Xia, W.; Luan, X.X.; Zhang, W.; Wu, D.F. Sulfuration of hierarchical Mn-doped NiCo LDH heterostructures as efficient electrocatalyst for overall water splitting. *Int. J. Hydrogen Energy* **2023**, *48*, 27631–27641. [[CrossRef](#)]
35. Ge, J.M.; Diao, S.T.; Jin, J.X.; Wang, Y.P.; Zhao, X.H.; Zhang, F.Z.; Lei, X.D. NiFeCu phosphides with surface reconstruction via the topotactic transformation of layered double hydroxides for overall water splitting. *Inorg. Chem. Front.* **2023**, *10*, 3515–3524. [[CrossRef](#)]
36. Wang, Y.F.; Ye, Q.; Lin, L.; Zhao, Y.X.; Cheng, Y.L. NiFeRu/C and Ru, Fe-Ni₅P₄/C as complementary electrocatalyst for highly efficient overall water splitting. *J. Colloid Interface Sci.* **2023**, *651*, 1008–1019. [[CrossRef](#)]
37. Karmakar, A.; Krishnan, A.V.; Jayan, R.; Madhu, R.; Islam, M.M.; Kundu, S. Structural modulation of low-valent iron in LDH-derived Ni₃Se₄ nanosheets: A breakthrough electrocatalyst for the overall water splitting reaction. *J. Mater. Chem. A* **2023**, *11*, 10684–10698. [[CrossRef](#)]
38. Xu, X.M.; Pan, Y.L.; Ge, L.; Chen, Y.B.; Mao, X.; Guan, D.Q.; Li, M.R.; Zhong, Y.J.; Hu, Z.W.; Peterson, V.K.; et al. High-Performance Perovskite Composite Electrocatalysts Enabled by Controllable Interface Engineering. *Small* **2021**, *17*, 2101573. [[CrossRef](#)]
39. Wang, H.M.; Feng, T.; Wang, L.C.; Hao, W.J. Quantum dot-doped CeO_x-NiB with modulated electron density as a highly efficient bifunctional electrocatalyst for water splitting. *Nanoscale* **2023**, *15*, 6321–6332. [[CrossRef](#)]
40. Xu, X.M.; Yang, K.F.; She, J.Z.; Zhai, Y.S.; Zhou, M.H.; Deng, R.H.; Li, Z.M.; Cai, H. Self-supporting and bifunctional Cu-based electrocatalysts with porous structures as superior working electrodes for alkaline water splitting. *CrystEngComm* **2023**, *25*, 1276–1285. [[CrossRef](#)]

Disclaimer/Publisher's Note: The statements, opinions and data contained in all publications are solely those of the individual author(s) and contributor(s) and not of MDPI and/or the editor(s). MDPI and/or the editor(s) disclaim responsibility for any injury to people or property resulting from any ideas, methods, instructions or products referred to in the content.